Supporting Information

Spin/Valley Coupled Dynamics of Electrons and Holes at the MoS_2-$MoSe_2$ Interface

Abhijeet Kumar[1], Denis Yagodkin[1], Nele Stetzuhn[1], Sviatoslav Kovalchuk[1], Alexey Melnikov[2], Peter Elliott[3], Sangeeta Sharma[3], Cornelius Gahl[1], and Kirill I. Bolotin[1,*]

[1]Department of Physics, Freie Universität Berlin, 14195 Berlin, Germany
[2]Institute for Physics, Martin Luther University Halle, 06120 Halle, Germany
[3]Max-Born-Institut für Nichtlineare Optik und Kurzzeitspektroskopie, Max-Born Straße 2a, 12489 Berlin, Germany

*kirill.bolotin@fu-berlin.de

Supplementary note 1: Upper limit of reflectivity and spin/valley polarization rise time

We approximate the overall dynamics in our heterostructure as that of a 3-level system where a pump pulse excites population from ground state-0 to excited state-1. This is followed by ultrafast charge transfer of the excited population (electrons or holes) from excited state-1 into the energy state-2, whose decay we probe in our system. Based on this approximation, we fit the dynamics with the convolution of two functions as following:

$$f(t) = \left[-A\exp\left(-\frac{t}{\tau_{rise}}\right) + A\exp\left(-\frac{t}{\tau_{decay}}\right)\right] * \frac{1}{\sigma\sqrt{2\pi}}\exp\left(-\frac{t^2}{2\sigma^2}\right) \quad \text{(SI 1)}$$

Here, the last term in (SI 1) is the instrument response, that is, the pump-probe correlation function. The full-width at half maximum of the pump-probe correlation function is defined as $\text{FWHM} = 2\sigma\sqrt{2\ln(2)}$. The value of FWHM at the output of our laser system is 270 fs. However, we expect a slight temporal broadening of the pulses at the sample position due to significantly long beam path through several optical elements. Expecting this deviation, our aim is to estimate the upper limit of rise time for Kerr and reflectivity signal. Assuming direct population transfer from state-0 to state-2, we first fit the reflectivity signal with a single exponential decay convolved with the Gaussian cross-correlation function and extract the upper limit of FWHM = 286 fs. A fit to the Kerr data in Fig. 2d (main text) using the fit function (SI 1) with FWHM = 286 fs gives us the upper limit of spin-valley polarization build-up time to be 170 ± 40 fs for holes and 250 ± 70 fs for electrons, respectively. By varying the FWHM within reasonable limits in our fitting procedure (± 5 fs), we estimate the upper limit of reflectivity rise time (Fig. 2d, main text) to be 40 fs for both electrons and holes.

Supplementary note 2: Evolution of Kerr and reflectivity signal in MoS_2

To investigate the time delay between the reflectivity and MOKE signals, we performed time-dependent density functional theory (TDDFT) linear response (LR) simulations for a MoS_2 monolayer. The tunneling process from $MoSe_2$ to MoS_2 in the heterostructure is modelled by the injection of electrons into the MoS_2 conduction band, and the changes in magneto-optical spectra are calculated.

In LR-TDDFT, the linear susceptibility, $\chi(\omega)$, is found by solving the Dyson-like equation[1]:

$$\chi(\omega) = \chi_S(\omega) + \chi_S(\omega)(v + f_{XC})\chi(\omega)$$

where $\chi_S(\omega)$ is the non-interacting Kohn-Sham (KS) susceptibility, v is the bare Coulomb interaction, and f_{XC} is the exchange-correlation (XC) kernel. The XC kernel must be approximated. From this susceptibility, the frequency-dependent dielectric tensor, ε(ω), and the Kerr rotation angle $\theta_K(\omega)$ can be calculated:

$$\varepsilon_{ij}^{-1}(\omega) = \delta_{ij} + v\chi_{ij}(\omega),$$
$$\theta_K(\omega) = -\frac{\varepsilon_{xy}(\omega)}{\sqrt{\varepsilon_{xx}(\omega)}\,(1 - \varepsilon_{xx}(\omega))}$$

The KS susceptibility can be calculated from the ground-state DFT energies ϵ_{nk}, the real-space orbitals $\phi_{nk}(r)$, and their occupations f_{nk}, where nk labels the state and k-point in reciprocal space:

$$\chi_S(r, r', \omega) = \sum_{nmk} (f_{nk} - f_{mk}) \frac{\phi_{nk}^*(r)\phi_{mk}^*(r')\phi_{nk}(r')\phi_{mk}(r')}{\omega - \epsilon_{nk} + \epsilon_{mk} + i\eta}$$

For insulators and semiconductors, the standard approximations for the XC kernel are known to have difficulty describing excitons. Hence we use a long-range corrected kernel, $f_{XC} = -\alpha/q^2$ with $\alpha = 2.0$, although the binding energy is strongly underestimated for 2D materials. This is due to the difficulty in describing 2D materials with functionals designed for 3D systems. However, we confirm that the physics is the same for several reasonable values of α. This difficulty for 2D materials also manifests itself in the large difference between the LDA KS gap and the fundamental gap, as calculated by the GW method.

As was shown in ref.[1], transient signals may be successfully calculated using non-equilibrium occupations, $f_{nk}(t)$. For this work, we compute two sets of occupations to model injected electrons and their subsequent relaxation to a Fermi-Dirac distribution. This is due to the prohibitive computational demands of a real-time calculation of the MoS_2-$MoSe_2$ heterostructure, as a large supercell is required to correctly describe the band ordering around the Fermi level, as well as the significant simulation time required to capture the relaxation dynamics.

For the injected case (INJ), the occupations above the fermi level were given by a Gaussian centered 400 meV above the lowest conduction band energy with width 100 meV and

amplitude 0.15 (chosen based on the occupation following a real-time TDDFT calculation for excitation with a laser with fluence $0.1 mJ/cm^2$). The relaxed case (RLX) occupations are given by a Fermi-Dirac distribution where the chemical potential and temperature are chosen so that the number of electrons and internal energy is the same as the injected case. The density of states for these two distributions can be seen in Supplementary Fig. S6.

Using the INJ and RLX occupations to construct the KS susceptibility allows us to calculate and compare the absorption and Kerr rotation angles for these two cases. The results are shown in Supplementary Fig. S7.

As can be seen in Supplementary Fig. S7, both the INJ and RLX cases show a similar change in the absorption spectra at the exciton frequency, while only the RLX case shows a change in the Kerr rotation angle at the frequency. Thus, the Kerr signal will lag behind absorption/reflectivity signal as the injected electrons must first relax to this transient thermal distribution in order to see a non-zero signal at the exciton frequency. This is also supported by our experimental observation of Kerr signal rise time being only weakly dependent on probe energy (Supplementary Fig. S8).

Explaining peaks in Kerr spectrum at low and high energy: We attribute the features near and below 1 eV (blue peaks in Supplementary Fig. S7) to the transition of injected electrons into the higher conduction bands. These higher bands also have spin-orbit splitting leading to spin polarization and a non-zero Kerr signal. We can confirm this aspect as these low energy peaks disappear when we remove the higher bands from the linear response calculations. Similarly, the peaks above 2 eV are due to the transitions from the spin-orbit split valance band states to the unoccupied states at the same energy at the injected electrons. Since the injected electrons are spin-polarized, there is an imbalance in the number of unoccupied states in each spin channel available for this excitation. Spin/valley polarization at higher energies while pumping near A-excitons in a monolayer TMD was previously studied experimentally[2]. The peaks below 0.2 eV in absorption and Kerr spectra are due to intraband transitions in the conduction band.

Computational parameters: All calculations performed using the ELK electronic structure code [elk.sourceforge.net]. The lattice parameters used were $a = 3.16 Å$ with a vacuum of 25.6Å and k-point grid of 30x30x1. There were 16 empty states per k-point. For the LR-TDDFT calculations, a smearing of 0.035 atomic units was used to broaden the peaks.

Supplementary note 3: Analysis of confounding effects

It is important to analyze confounding effects other than spin/valley- and charge- relaxation that could potentially contribute to our experiments. These effects include energy transfer, intralayer excitation of monolayers, interlayer exciton exchange interaction, photo carrier diffusion, etc. The appearance of a transient reflectivity signal in one material of the heterostructure after the excitation of the other material (e.g. Fig. 2,3 in the main text) could result from the transfer of energy[3] or charge[4] across the MoS_2-$MoSe_2$ interface. Energy transfer is forbidden in the case of pumping the lower bandgap material $MoSe_2$. For the case of pumping MoS_2, energy transfer in principle is allowed. However, since energy transfer is unlikely to conserve spin, the main effect of this process on the Kerr signal would be a reduction of our total Kerr amplitude without changing the picosecond dynamics. Additionally, any possible energy transfer would be immediately followed by fast charge transfer bringing electrons back into MoS_2 and holes into $MoSe_2$. We conclude that the transient optical signals are dominated by photoexcited holes transferred across the heterostructure interface upon pumping MoS_2, and electrons upon pumping $MoSe_2$.

As noted earlier, a pump resonant with the MoS_2 bandgap also non-resonantly excites the lower-bandgap material $MoSe_2$. However, our signals are not significantly affected by intralayer dynamics in $MoSe_2$. This is confirmed by i) the lack of Kerr signal for non-resonant excitation of monolayer $MoSe_2$ (Supplementary Fig. S2d, S2e) and ii) approximately 7 times weaker reflectivity signal in monolayer $MoSe_2$, that vanishes within 20 ps after photoexcitation compared to the heterostructure region (Supplementary Fig. S2b, 2c). In addition, we do not observe any dependence of the reflectivity dynamics on pump fluence (Supplementary Fig. S3) which would be expected for intralayer dynamics in TMDs[5,6].

Laser-induced changes in temperature of the heterostructure could also influence the relaxation dynamics. Such temperature-related effects are also ruled out by the lack of pump fluence dependence. Finally, photoexcited carriers could potentially diffuse out of the probe spot during their lifetime. However, this effect is likely insignificant in our system since we can estimate the diffusion length to be <10 nm within our observed lifetime[7].

We note that the excitonic nature of indirect electron-hole pairs could manifest in the spin/valley dynamics at cryogenic temperature. However, the rate of spin scattering due to interlayer electron-hole exchange interaction is expected to be lower compared to that of previously considered intravalley and intervalley scattering[8]. For contrasting spin/valley dynamics of electrons and holes, with similar population lifetimes, <1 ns, the role of intervalley and intravalley scattering is predominant in our devices.

Supplementary note 4: Methods

Sample preparation

Individual MoS_2 and $MoSe_2$ flakes were mechanically exfoliated on a PDMS (polydimethylsiloxane) substrate and subsequently transferred onto a SiO_2/Si substrate using a well-established dry-transfer technique[9] without controlling the stacking angle. The heterostructure samples were vacuum annealed at 200°C for 30 minutes to improve interlayer coupling. Overall, 6 samples were fabricated and measured.

Pump-probe spectroscopy

The samples placed inside a cryostat were measured at a base temperature of 4.2 K. The cryostat was mounted on a motor-controlled xy-translation stage with sub-micrometer spatial resolution. We used a wavelength-tunable femtosecond pulsed laser system (Coherent Chameleon Ultra II + compact OPO-VIS) with sub-200 fs pulse duration and 80 MHz repetition rate. Fine tuning in the pump/probe energy was done to optimize the Kerr signal. Both pump and probe pulses were focused into a roughly 1 μm^2 spot on the sample at normal incidence. The pump fluence was varied between $10\ \mu J/cm^2$ and $100\ \mu J/cm^2$ in our experiments. The reflected linearly polarized probe was passed through an optical bridge consisting of a half-wave plate and a Wollaston prism, which separates the beam into two components of orthogonal polarization. Both signals were recorded by using a balanced photodetector and a lock-in amplifier phase-locked to a chopper in the pump path. The Kerr and reflectivity signals were normalized with respect to the static probe reflectivity; normalization to the time-dependent reflectivity produces identical results.

Low T PL measurements

For low T PL measurements, we used another optical setup (Witec Alpha confocal spectroscopy setup) with a Nikon 50×SLWD objective of NA = 0.5. Samples were placed in a cryostat at 5 K. The laser excitation wavelength was set to 532 nm and 633 nm to access the spectral range of MoS_2 and $MoSe_2$, respectively. The laser power was varied within 20 μW and 30 μW.

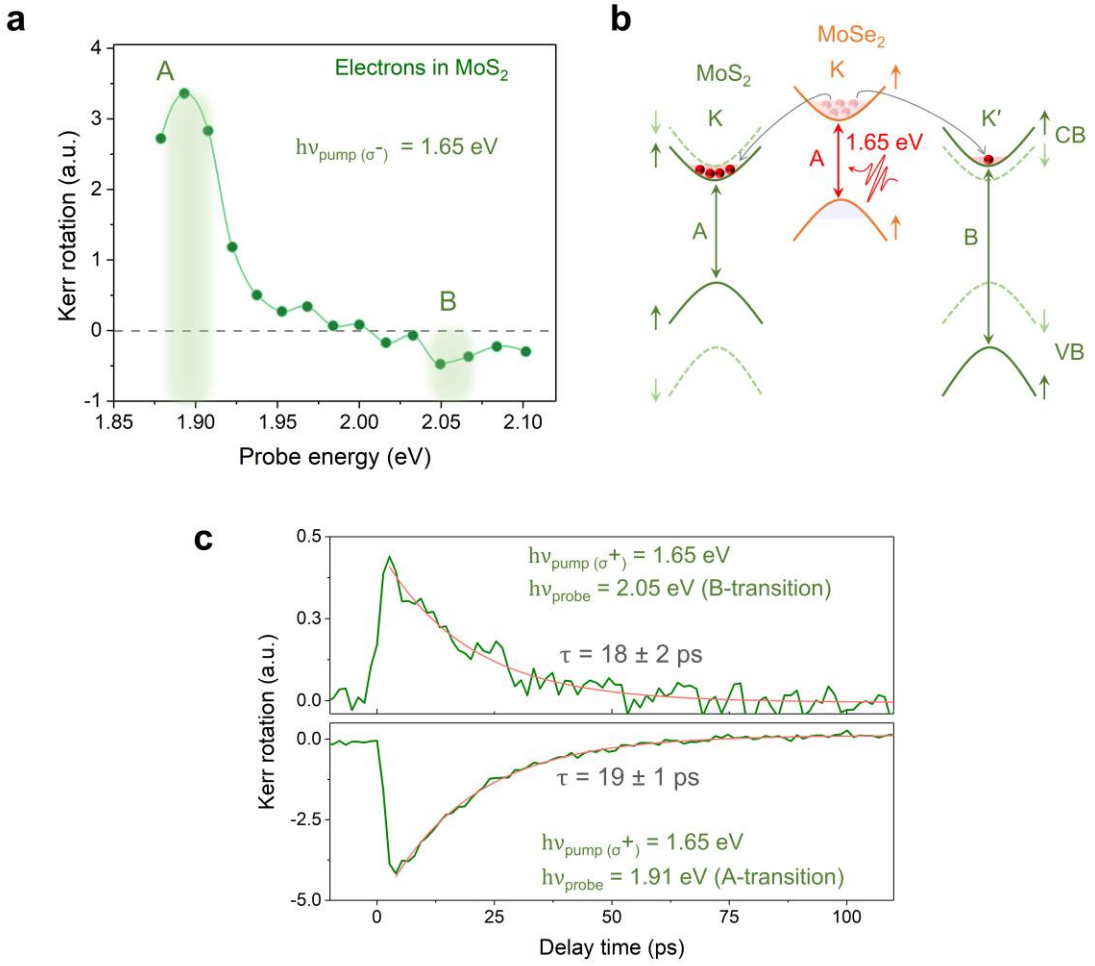

Supplementary figure S1: Comparison of spin/valley dynamics between conduction sub-bands of MoS_2. (a) Kerr rotation angle vs. probe photon energy (in the region of MoS_2 absorption) at 2 ps delay for pump corresponding to the $MoSe_2$ optical bandgap (1.65 eV). The heterostructure sample is different from the one presented in the main text. Kerr signal flips its sign between probe energies corresponding to the transition into lower conduction sub-band (A transition, ~1.90 eV) and the higher conduction band sub-band (B transition, ~2.05 eV) in MoS_2. **(b)** Schematic diagram for tunneling of spin-polarized electrons from $MoSe_2$ into MoS_2 conduction bands. **(c)** Time-resolved Kerr dynamics probed near B transition (upper panel) and near A transition (lower panel) in MoS_2. Similar dynamics of both traces suggest equally fast depolarization of electrons in the higher and the lower conduction sub-bands.

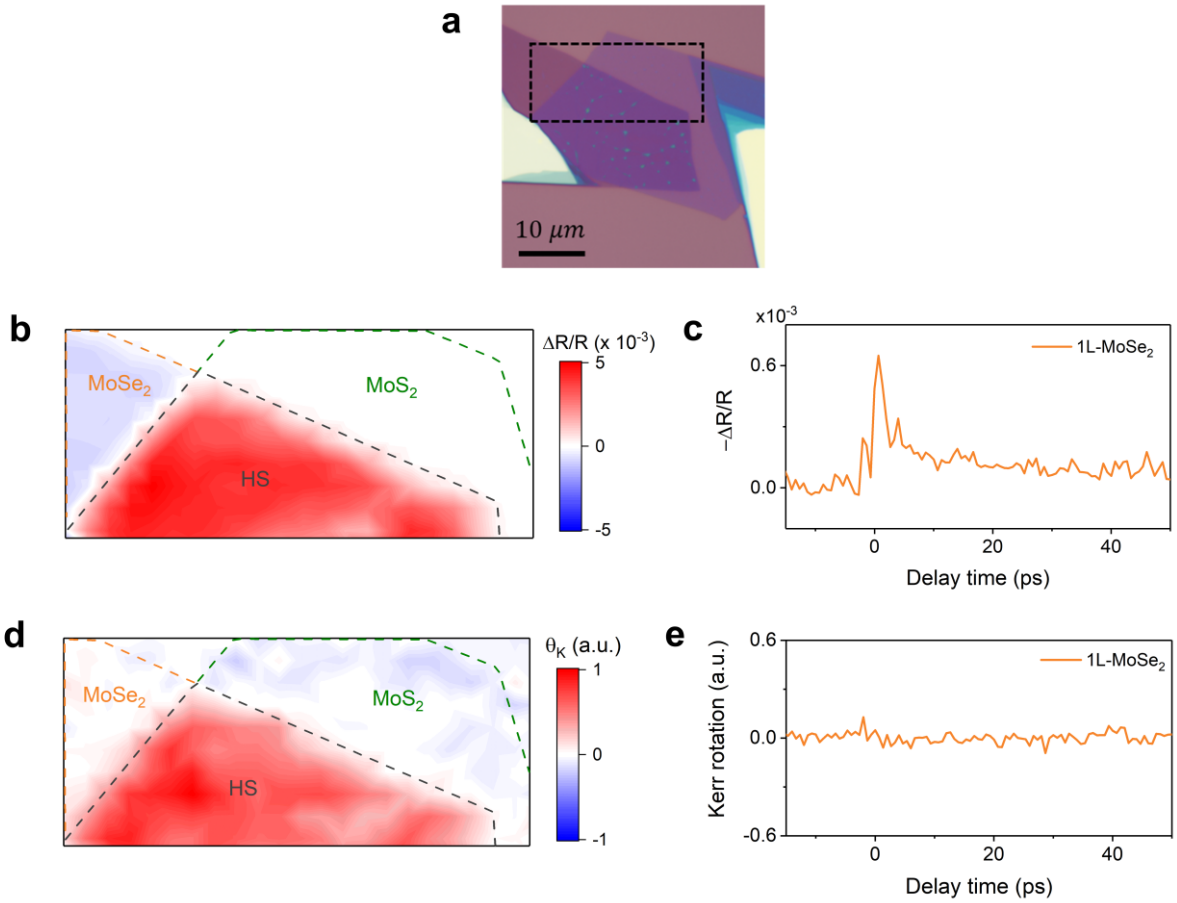

Supplementary figure S2: Spin/valley and population dynamics in $MoSe_2$ under non-resonant excitation. (a) Optical image of MoS_2-$MoSe_2$ heterostructure (same device as in the main text). Dashed line marks the region of maps in b) and d). Kerr and reflectivity maps/traces were recorded under pumping at 1.94 eV (optical bandgap of MoS_2) and probing at 1.62 eV (optical bandgap of $MoSe_2$). In addition to the excitation of MoS_2 and probing of $MoSe_2$ considered in the main text, these conditions also result in non-resonant excitation of lower bandgap material $MoSe_2$. **(b)** Spatial reflectivity map across the region marked in a) at 2 ps delay. Note the complete lack of the reflectivity signal from the monolayer MoS_2 region and approximately seven times weaker signal with opposite sign from the monolayer $MoSe_2$ region compared to the heterostructure. **(c)** Time-resolved reflectivity trace from the isolated $MoSe_2$ region. This signal is weak and decays completely within 20 ps. **(d)** Corresponding Kerr map. Note that no Kerr signal is observed from the monolayer regions. **(e)** Time-resolved Kerr trace from the isolated monolayer $MoSe_2$ region. No dynamics are observed.

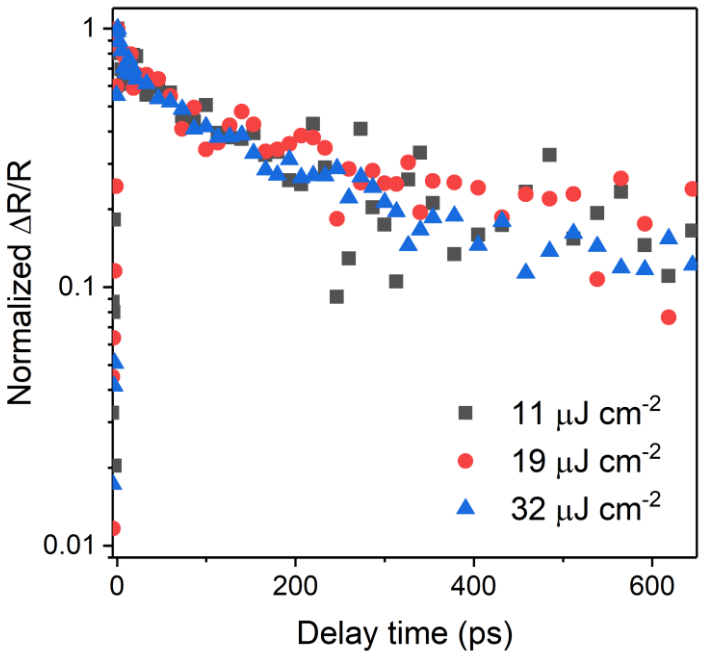

Supplementary figure S3: Pump fluence dependence of hole population dynamics. Hole population dynamics in the MoS_2-$MoSe_2$ heterostructure for three different pump fluence. Pump energy is fixed to 1.88 eV, while the probe energy is tuned to 1.59 eV, near optical bandgap of $MoSe_2$. No significant variation on the population dynamics of holes is observed. This rules outs the contribution of intralayer dynamics in $MoSe_2$, which is expected to be significantly affected by exciton-exciton annihilation mechanism.

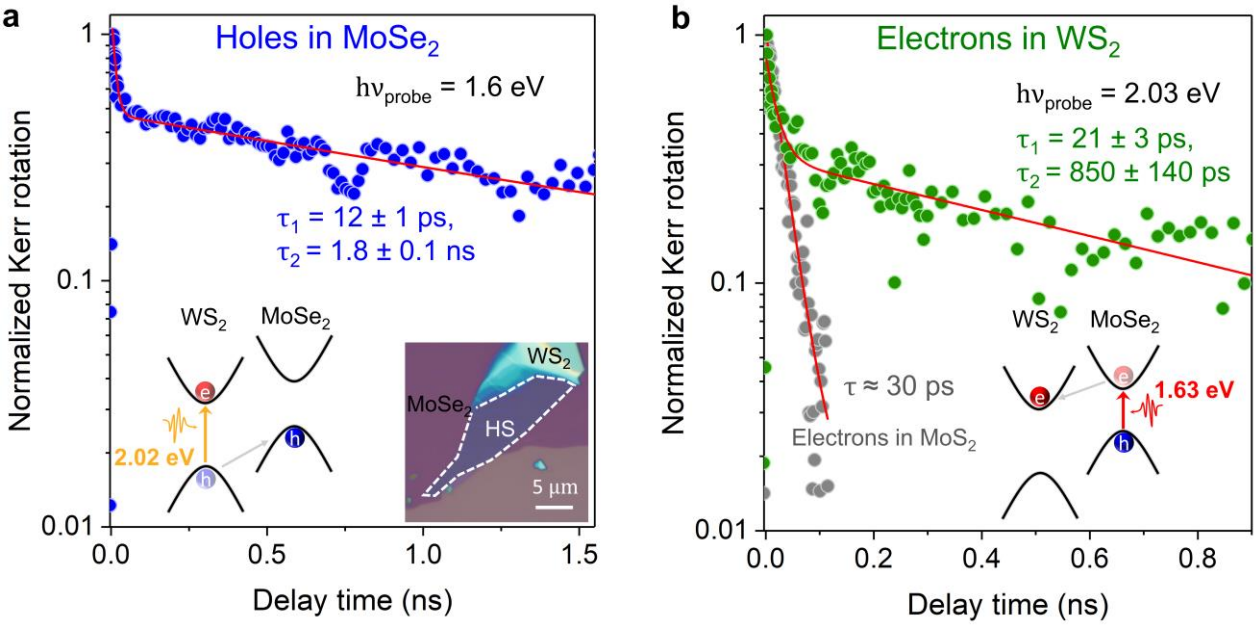

Supplementary figure S4: Comparison of spin/valley dynamics between electrons and holes in WS_2-$MoSe_2$ heterostructure. (a) The tunneled spin-polarized holes in $MoSe_2$ (upon photoexcitation near WS_2 bandgap) show long spin/valley lifetime similar to the case of MoS_2-$MoSe_2$ heterostructure. The optical image of WS_2-$MoSe_2$ heterostructure is shown in inset (bottom-right). **(b)** The tunneled spin-polarized electrons in WS_2 show significantly different dynamics (green points) compared to the previously studied case of electrons in MoS_2 (gray points, same data as in Fig. 3b in main text).

This disparity between electron dynamics in WS_2 and MoS_2 can be ascribed to a larger spin-orbit splitting of the conduction band in WS_2 (27 meV compared to 3 meV in MoS_2) and optically forbidden dark transition associated with the lower conduction sub-bands in WS_2.

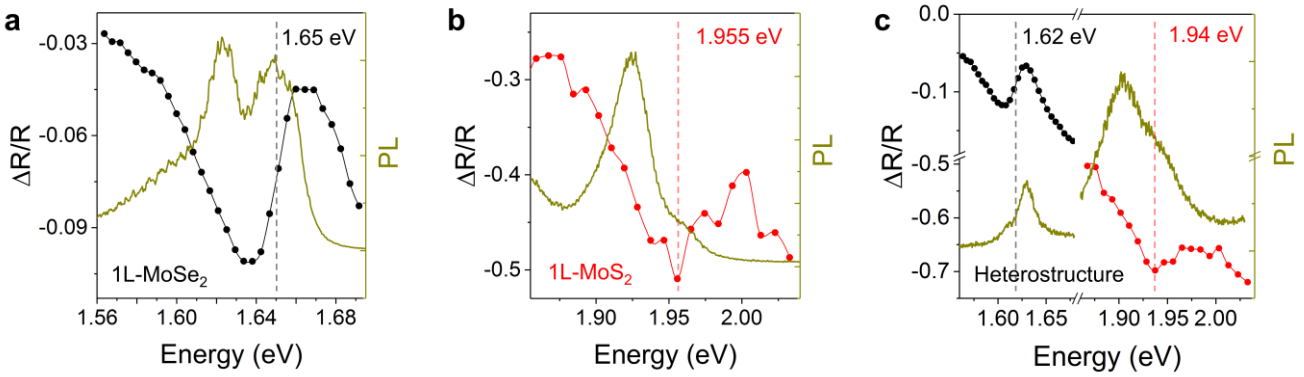

Supplementary figure S5: Differential reflectivity spectra of MoS_2-$MoSe_2$ at 6K. Differential reflectivity spectra of **(a)** monolayer $MoSe_2$, **(b)** monolayer MoS_2, and **(c)** heterostructure region of the same device as in the main text (black and red curves). The measurements were carried out using the same tunable laser system we obtained the rest of the data in the manuscript. The finite spectral width of our femtosecond laser system (8 meV around $MoSe_2$ excitons, 38 meV around MoS_2 excitons) limits the spectral resolution of these measurements. Nevertheless, we observe a fano-like dispersive transition near 1.65 eV for monolayer $MoSe_2$ and near 1.62 eV in the heterostructure representing the excitonic absorption in the region. For MoS_2 spectral range, we observe a dip near 1.955 eV in the monolayer region and near 1.94 eV in the heterostructure. These spectral positions match well with the PL data from the same sample (yellow curves, same data as in Fig. 1d, main text). The dashed lines show approximate positions of excitonic resonances.

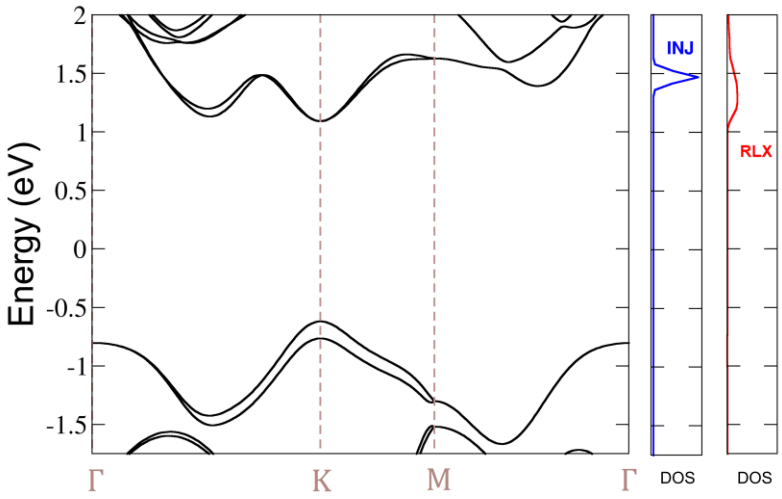

Supplementary figure S6: Band structure in MoS_2 and change in density of states upon spin injection. The band structure of monolayer MoS_2 around the Fermi level (set to 0 eV) and the change in the density of states from the ground-state due to the injected (INJ) electrons and the relaxed (RLX) electrons.

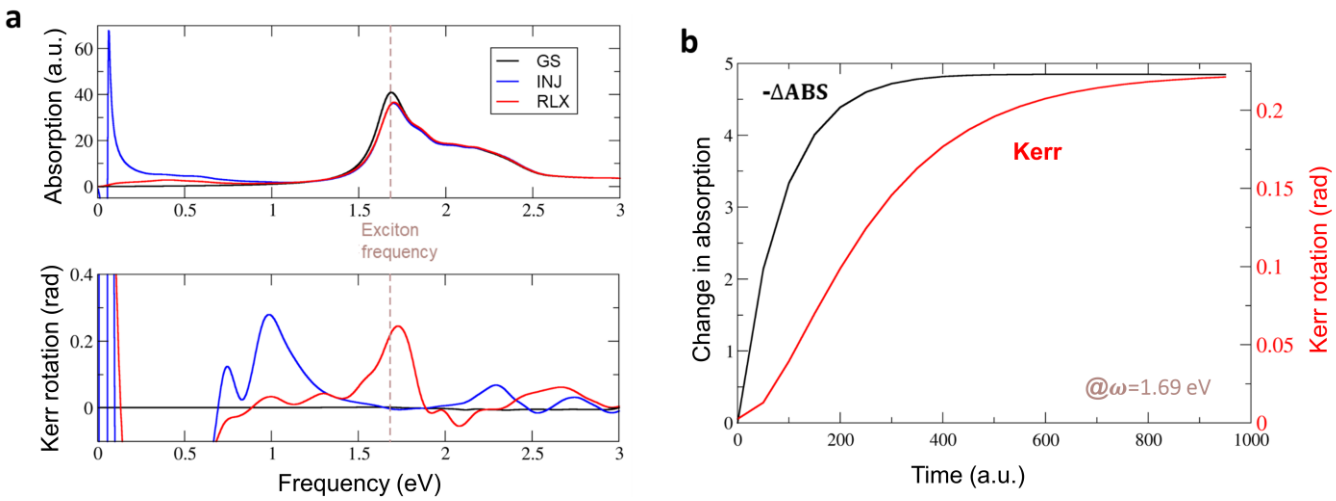

Supplementary figure S7: Simulated absorption and Kerr response in MoS_2. (a) The absorption (upper panel) and Kerr spectra (lower panel) for the ground-state (GS), injected electrons (INJ), and relaxed electron (RLX) cases calculated with TDDFT using the LRC XC kernel. A dashed line marks the exciton peak near 1.69 eV. **(b)** The absorption and Kerr signal rise (probed at 1.69 eV) are obtained by interpolating the occupation between GS, INJ, and RLX limits from (a). A delay between the Kerr and absorption signal is clearly visible. We use differential equations for the electrons in INJ and RLX states with simple exponential decay constants for both the injection and relaxation processes (with the time constant of relaxation twice that of injection) to produce occupations at different times. These KS occupations are then used for LR-TDDFT calculation to find the absorption change and Kerr angle at each time.

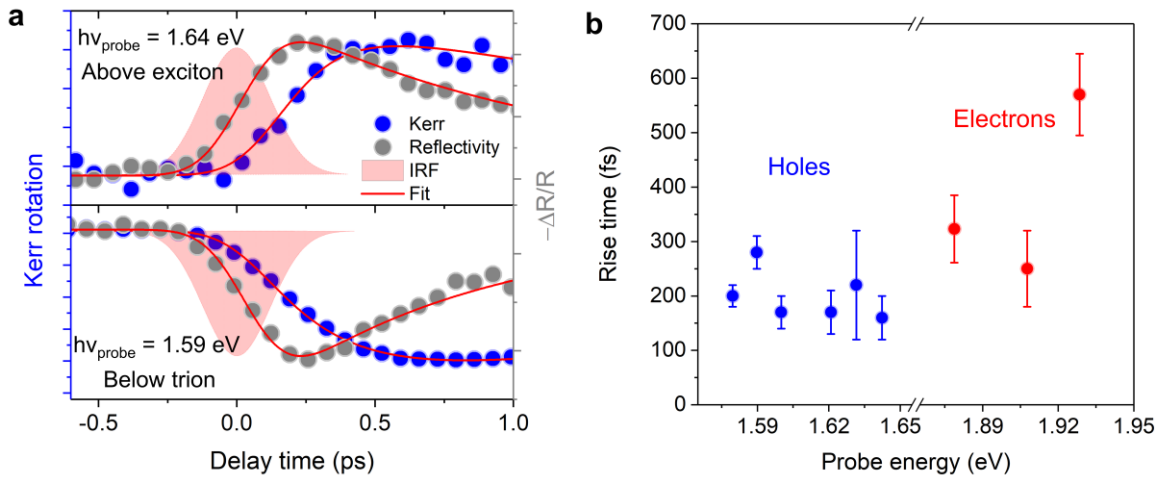

Supplementary figure S8: Probe energy dependent Kerr signal rise time. (a) Time evolution of Kerr and reflectivity signals for holes at two different probe energies. The Kerr rise time is significantly slower than the reflectivity rise time for both probe energies. **(b)** Kerr rise time extracted from the fit to Kerr signals of electrons (red) and holes (blue) in MoS_2-$MoSe_2$ heterostructure through the spectral range around exciton-trion transitions. The observed Kerr rise time is in 100s of femtoseconds across multiple probe energies. We observe slightly slower Kerr signal rise of electrons compared to the holes that could be attributed to contrasting spin splitting in the conduction and valance bands. While hot electrons can scatter in between the higher and lower conduction sub-bands in MoS_2, the tunneled holes predominantly cool down in the higher valance sub-band in $MoSe_2$.

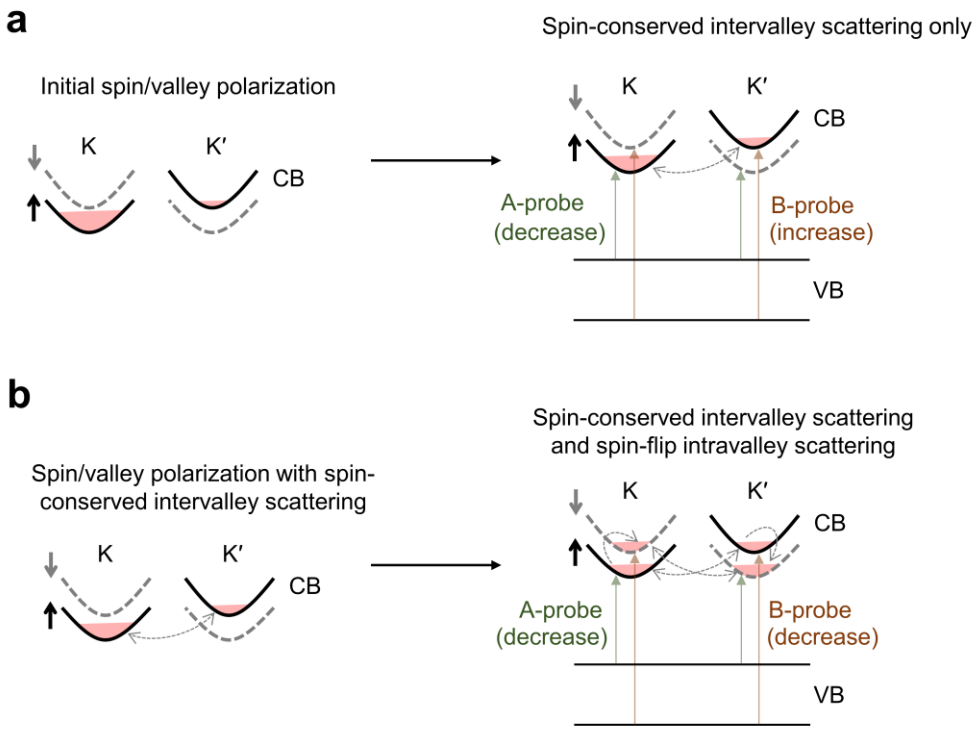

Supplementary figure S9: Spin/valley depolarization of electrons in MoS_2 conduction band. (a) Initial spin/valley polarization (for the case of spin-up tunneled electrons) in MoS_2 conduction band (left). Complementary kinetics of spin/valley polarization in the two sub-bands (A- and B-probe, respectively) when only spin-conserved intervalley scattering occurs (right). Kerr rotation signal at A-probe (B-probe) will decrease (increase). **(b)** Spin/valley polarization with contribution of fast spin-conserved intervalley scattering (left). Spin/valley depolarization governed by both spin-conserving intervalley scattering and spin flip intravalley scattering (right). This will decrease the spin/valley polarization in both sub-bands. Finally, the spin/valley depolarization in both the sub-bands is determined by the efficiency of spin-flip intravalley scattering.

Device #	Stacking (top-bottom)	Electron spin lifetime	Hole spin lifetime
1	MoS_2-$MoSe_2$	13 ± 2 ps	39 ± 14 ps; 180 ± 8 ps
2	$MoSe_2$-MoS_2 (main text)	28 ± 1 ps	38 ± 3 ps; 640 ± 70 ps
3	MoS_2-$MoSe_2$ (F_4TCNQ doped)	54 ± 1 ps	13 ± 3 ps; 179 ± 14 ps
4	MoS_2-$MoSe_2$	37 ± 2 ps	35 ± 3 ps; 830 ± 53 ps
5	MoS_2-$MoSe_2$	42 ± 3 ps	--
6	$MoSe_2$-MoS_2	19 ± 1 ps	--

Supplementary table 1: Sample variation of spin/valley dynamics. We performed measurements across 6 different samples. All samples were fabricated via mechanical exfoliation followed by dry-transfer without controlling the stacking angle. We observe similar behavior between spin dynamics of electrons and holes across these samples. Our results confirm that stacking order and stacking angle do not significantly affect the spin dynamics in our heterostructures. Sample #3 was covered with drop casted F_4TCNQ molecules, which are electron acceptors and induce p-doping in the sample[10]. We observe a slight change in relative spin lifetimes between electrons and holes, and conclude that it will be interesting to investigate spin dynamics in TMD heterostructures under controlled doping.

References:

(1) Dewhurst, J. K.; Willems, F.; Elliott, P.; Li, Q. Z.; Schmising, C. V. K.; Strüber, C.; Engel, D. W.; Eisebitt, S.; Sharma, S. Element Specificity of Transient Extreme Ultraviolet Magnetic Dichroism. *Phys. Rev. Lett.* **2020**, *124*, 077203.

(2) Yan, T.; Yang, S.; Li, D.; Cui, X. Long Valley Relaxation Time of Free Carriers in Monolayer WSe_2. *Phys. Rev. B* **2017**, *95*, 241406.

(3) Kozawa, D.; Carvalho, A.; Verzhbitskiy, I.; Giustiniano, F.; Miyauchi, Y.; Mouri, S.; Castro Neto, A. H.; Matsuda, K.; Eda, G. Evidence for Fast Interlayer Energy Transfer in $MoSe_2$/WS_2 Heterostructures. *Nano Lett.* **2016**, *16* (7), 4087–4093.

(4) Ceballos, F.; Bellus, M. Z.; Chiu, H. Y.; Zhao, H. Ultrafast Charge Separation and Indirect Exciton Formation in a MoS_2-$MoSe_2$ van Der Waals Heterostructure. *ACS Nano* **2014**, *8* (12), 12717–12724.

(5) Kumar, N.; Cui, Q.; Ceballos, F.; He, D.; Wang, Y.; Zhao, H. Exciton-Exciton Annihilation in $MoSe_2$ Monolayers. *Phys. Rev. B - Condens. Matter Mater. Phys.* **2014**, *89* (12), 125427.

(6) Yu, Y.; Yu, Y.; Xu, C.; Barrette, A.; Gundogdu, K.; Cao, L. Fundamental Limits of Exciton-Exciton Annihilation for Light Emission in Transition Metal Dichalcogenide Monolayers. *Phys. Rev. B* **2016**, *93* (20), 201111.

(7) Harats, M. G.; Kirchhof, J. N.; Qiao, M.; Greben, K.; Bolotin, K. I. Dynamics and Efficient Conversion of Excitons to Trions in Non-Uniformly Strained Monolayer WS_2. *Nat. Photonics* **2020**, *14* (5), 324–329.

(8) Rivera, P.; Seyler, K. L.; Yu, H.; Schaibley, J. R.; Yan, J.; Mandrus, D. G.; Yao, W.; Xu, X. Valley-Polarized Exciton Dynamics in a 2D Semiconductor Heterostructure. *Science.* **2016**, *351* (6274), 688–691.

(9) Castellanos-Gomez, A.; Buscema, M.; Molenaar, R.; Singh, V.; Janssen, L.; Van Der Zant, H. S. J.; Steele, G. A. Deterministic Transfer of Two-Dimensional Materials by All-Dry Viscoelastic Stamping. *2D Mater.* **2014**, *1* (1), 011002.

(10) Wang, J.; Ji, Z.; Yang, G.; Chuai, X.; Liu, F.; Zhou, Z.; Lu, C.; Wei, W.; Shi, X.; Niu, J.; Wang, L.; Wang, H.; Chen, J.; Lu, N.; Jiang, C.; Li, L.; Liu, M. Charge Transfer within the F4TCNQ-MoS_2 van Der Waals Interface: Toward Electrical Properties Tuning and Gas Sensing Application. *Adv. Funct. Mater.* **2018**, *28* (51), 1806244.